APPLIED PHYSICS

Emergence of a real-space symmetry axis in the magnetoresistance of the one-dimensional conductor $Li_{0.9}Mo_6O_{17}$

Jianming Lu[1,2]*†, Xiaofeng Xu[3]*, M. Greenblatt[4], R. Jin[5], P. Tinnemans[2], S. Licciardello[1,2], M. R. van Delft[1,2], J. Buhot[1,2], P. Chudzinski[6], N. E. Hussey[1,2]‡

We report on an emerging symmetry axis in the magnetoresistance of bulk single crystals of quasi–one-dimensional $Li_{0.9}Mo_6O_{17}$ below T_{min} = 25 K, the temperature at which the electrical resistivity experiences a minimum. Detailed angle-dependent magnetoresistance sweeps reveal that this symmetry axis is induced by the development of a negative magnetoresistance, which is suppressed only for magnetic fields oriented along the poles of the MoO_6 octahedra that form the conducting chains. We show that this unusual negative magnetoresistance is consistent with the melting of dark excitons, composed of previously omitted orbitals within the t_{2g} manifold that order below T_{min}. The unveiled symmetry axis in directional magnetic fields not only provides evidence for the crystallization of these dark excitons but also sheds new light on the long-standing mystery of the metal-insulator transition in $Li_{0.9}Mo_6O_{17}$.

INTRODUCTION

Magnetoresistance (MR) effects have been of immense interest in the condensed matter community in recent years, with the observation of colossal or extreme MR in topological semimetals (*1*–*3*), negative longitudinal MR in Weyl semimetals (*4*, *5*), and linear MR in a variety of systems (*2*, *6*–*8*). In this work, we report the discovery of a previously unidentified phenomenon in the magnetoresistive response of a one-dimensional (1D) metal whereby the angle dependence of the MR decouples from the crystalline axes. In essence, this emergence of an asymmetric MR can be ascribed to a crossover from an angular MR that is determined by the itinerant plane waves associated with the 1D Fermi surface aligned with the reciprocal lattice vectors, to one in which the local atomic basis becomes the new paradigm.

The material in question is the purple bronze $Li_{0.9}Mo_6O_{17}$ (LMO) (*9*), a quasi-1D metal hosting a particularly robust Tomonaga-Luttinger liquid (TLL) state—the 1D analog of the Fermi liquid for an interacting electron system (*10*). At high temperatures, both spectroscopic (*11*, *12*) and transport (*13*) measurements have provided evidence for TLL physics, including signatures of spin-charge separation. Below a certain temperature $T_{min} \sim 25$ K, the resistivity passes through a minimum (*14*) and begins to rise sharply before, finally, superconductivity sets in below around 2 K, possibly with an unconventional pairing symmetry (*15*). Despite three decades of experimental effort (*16*–*22*), the underlying mechanism of this resistive upturn remains elusive: There is no accompanying structural distortion (*23*), no signature of magnetic order (*24*), disorder can be ruled out by the presence of an anisotropic superconducting phase (at the lowest temperatures) (*15*), while the transition to a more insulating state excludes the simple dimensional crossover scenario (*25*). Moreover, the lack of any clear signal of a standard Peierls phase transition [e.g., in the specific heat (*16*, *22*)] suggests an exotic, higher-order transition that involves only a small fraction of the carriers. All this makes LMO exceptional among the family of bronzes.

Many aspects of this unusual phenomenon, described in more detail below, are found to be consistent with a new theoretical framework (*26*) for LMO in which dark excitons (*27*), formed within the t_{2g} manifold close to the Fermi level, order at T_{min} and, through their interaction with the charge carriers, induce the upturn in the resistivity. Both the anomalous angular dependence of the MR and the peculiar two-stage character of an underlying order-by-disorder phase transition suggest new physics involving multiorbital degrees of freedom.

RESULTS

LMO has a monoclinic crystal structure ($P2_1/m$) (*16*, *28*), with a primitive unit cell comprising two stacks of four corner-sharing MoO_6 octahedra and two MoO_4 tetrahedra arranged along a chain (see Fig. 1A). Although it is 3D in structure, electronically (for a doublet of bands crossing the Fermi energy), it is 1D due to the very weak orbital overlap between different stacks within the *ac* plane (*29*–*31*). As highlighted in purple in Fig. 1A, only two of the four MoO_6 octahedra are believed to have partially occupied *d*-shells that can contribute to the electrical conduction, which proceeds along the zigzag chain that extends in the crystallographic *b*-direction (Fig. 1B). Correspondingly, along Γ-X (see Fig. 1C) and Γ-Z (not shown), the interchain dispersion is almost negligible. A cut along the P-K line is shown in the lower panel of Fig. 1C. Because of the strong crystal field effects, the two bands crossing the Fermi level (one for each stack) are of d_{xy} character, while the d_{xz} and d_{yz} orbitals within the same manifold are either empty or fully occupied, with a minimum gap of around 0.4 eV (highlighted in green in Fig. 1C) located midway along the P-K line. (This particular aspect of the band structure will become important

[1]High Field Magnet Laboratory (HFML-EMFL), Radboud University, Toernooiveld 7, Nijmegen 6525 ED, Netherlands. [2]Institute for Molecules and Materials, Radboud University, Nijmegen 6525 AJ, Netherlands. [3]Advanced Functional Materials Lab and Department of Physics, Changshu Institute of Technology, Changshu 215500, China. [4]Department of Chemistry and Chemical Biology, Rutgers University, Piscataway, NJ 08854, USA. [5]Department of Physics and Astronomy, Louisiana State University, 229-B Nicholson Hall, Tower Dr., Baton Rouge, LA 70803-4001, USA. [6]School of Mathematics and Physics, Queen's University Belfast, University Road, Belfast, NI BT7 1NN, UK.
*These authors contributed equally to this work.
†Present address: State Key Laboratory for Mesoscopic Physics, Department of Physics, Peking University, Beijing 100871, China.
‡Corresponding author. Email: nigel.hussey@ru.nl

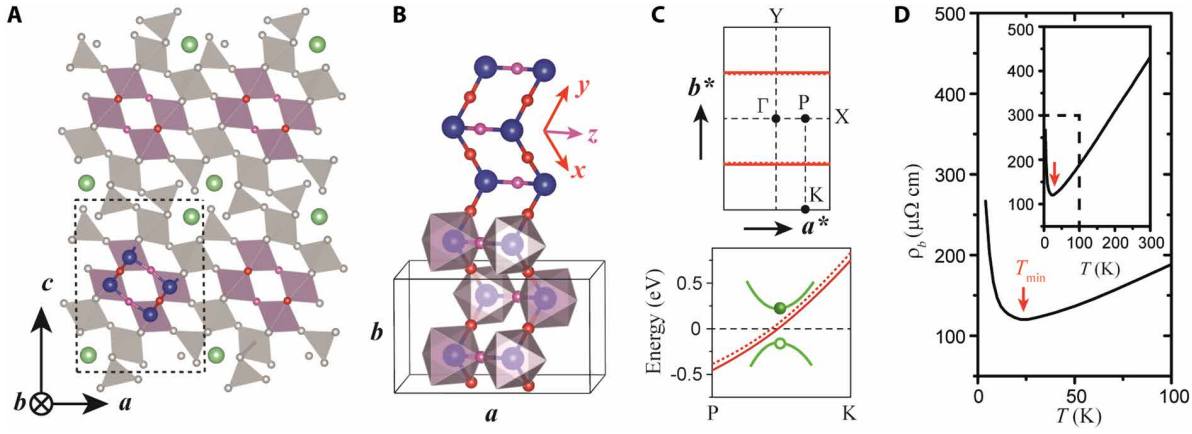

Fig. 1. Crystal structure, band structure, and metal-insulator transition of LMO. (**A**) Projection of four unit cells onto the *ac* plane, where the MoO_6 octahedra hosting the conducting zigzag chains (oriented out of this plane along the *b* axis) are highlighted in purple. Blue sphere, Mo; red/pink, O; green, Li. (**B**) In each unit cell, there are double zigzag chains made of corner-sharing octahedra. The octahedra at the top of the figure have had all nonessential oxygen atoms removed. The corner oxygen shared by adjacent in-chain octahedra is denoted in red, while interchain oxygen is denoted in pink. (**C**) Simplified Fermi surface of LMO showing the weakly dispersive, quasi-1D bands along the *a* axis due to the weak interchain hopping energy (top panel), which, nevertheless, causes an energy gap around the Fermi surface (schematic green curves in the lower panel). The small energy gap easily allows excitation of electron-hole pairs, i.e., excitons. (**D**) In-chain resistivity versus temperature showing a metal-insulator transition around T_{min} ~ 25 K, below which the insulating form of the resistivity can be well fitted by a power law (see section S4C and fig. S11). Crystallographic drawings were produced using VESTA (*44*).

later.) Last, Fig. 1D shows a typical in-chain resistivity curve $\rho_b(T)$. The upturn in $\rho_b(T)$ occurs around T_{min} ~ 25 ± 5 K, irrespective of whether the ground state is superconducting. Above T_{min}, the metallic behavior is usually ascribed to TLL physics, whereas the nonmetallic state below T_{min} has remained a mystery.

To gain more insight into the nature of the electronic state below T_{min}, we have investigated the angle-dependent MR (ADMR) in LMO for different current (*I*) and magnetic field (*B*) configurations (details of the resistivity measurements can be found in Materials and Methods). The angles of orientation of *B* within the three principal planes colored in Fig. 2A are specified by θ, α, and β throughout the manuscript. Figure 2B shows the temperature evolution of the angular dependence of the *a* axis MR (i.e., *I*//*a*) as a constant field of 13 T is rotated within the *ac* plane. Above T_{min} ~ 25 K, the MR has minima and maxima whenever the field is oriented along *a* or *c*, respectively. As shown in the left-hand panel of Fig. 2C, upon reflecting the MR trace about **B**//*c*, the two traces are perfectly superimposed, implying a fully symmetric response. With decreasing temperature however, the positions of the maxima (and, to a lesser extent, the minima) begin to shift away from the crystallographic axes. The developing asymmetry is most illustrated in the reflection plot, shown in the right-hand panel of Fig. 2C for *T* = 4.2 K. (Corresponding reflection plots for a number of intermediate temperatures are displayed in fig. S1.)

In general, the MR of a monoclinic crystal is asymmetric, with respect to the crystallographic axes (*32*). However, the inclined angle in LMO is so small (~0.61°) that the system can be taken to be orthorhombic within experimental uncertainty. This agrees well with the experimentally observed mirror symmetry of MR at high temperature and with the theoretically calculated Fermi surface (*30*). The unexpected breaking of the mirror symmetry at low temperature, nonetheless, points to a marked change in the electronic structure that can be enhanced by strong magnetic fields.

To quantify this unusual asymmetric response, we plot in Fig. 2D the integrated area (shaded area in the right-hand panel of Fig. 2C) between the two reflections normalized to the magnitude of the MR (i.e., the difference between the resistivity values at **B**//*c* and **B**//*a*). The inset in Fig. 2D shows a blowup of the region between 10 and 40 K. A clear onset in the asymmetry is revealed at a temperature T_{asym} = 24 ± 1 K, implying that it is intimately connected to the resistivity upturn at T_{min}. Moreover, the growth in the asymmetry near T_{min} resembles that of an order parameter. Below 10 K however, the asymmetry grows much more steeply (see the main panel of Fig. 2D for *I*//*a*, and fig. S2 for corresponding data for *I*//*b*).

This asymmetric MR is found to be independent of current direction. Figure 2E shows the evolution of the ADMR within the *ac* plane for *I*//*b* (similar data for *I*//*c* are shown in fig. S3). Above T_{min}, the mirror symmetry is preserved with respect to the crystallographic axes. Below T_{min}, the asymmetric behavior is observed at all temperatures. The magnitude of the asymmetry, however, does depend on the field strength. Fig. 2F shows the enhanced asymmetry with increasing field up to 30 T measured on a different LMO crystal at *T* = 1.2 K (see almost identical behavior in Fig. 3B for another insulating crystal and in fig. S6b for a second, superconducting crystal). As the field increases, the position of the maximum MR shifts away from the crystallographic axes. Notably, when the magnetic field is rotated within the *ab* or *bc* plane, there is no discernible shift in the position of the maxima/minima across T_{min} (see also figs. S3 and S4). No shift is found either with increasing field strength (fig. S5). Such a dependence of the asymmetric MR on the specific plane of rotation places strong constraints on any effective theory put forward to explain this effect.

To gain deeper insight into how the asymmetry develops with increasing *B*-field, we have performed a series of MR sweeps as a function of magnetic field oriented at multiple angles within the *ac* plane. Fig. 3A shows results for a nonsuperconducting sample mounted with *I*//*a* at *T* = 1.2 K. (Again, almost identical behavior in a superconducting sample is plotted in fig. S6). In the low-*B* regime (*B* < 5 T), Δρ(*B*) follows a quadratic dependence in field and scales approximately as *B*cosθ (θ measured from the *c* axis), albeit with a small negative offset, suggesting that it originates from the effects of

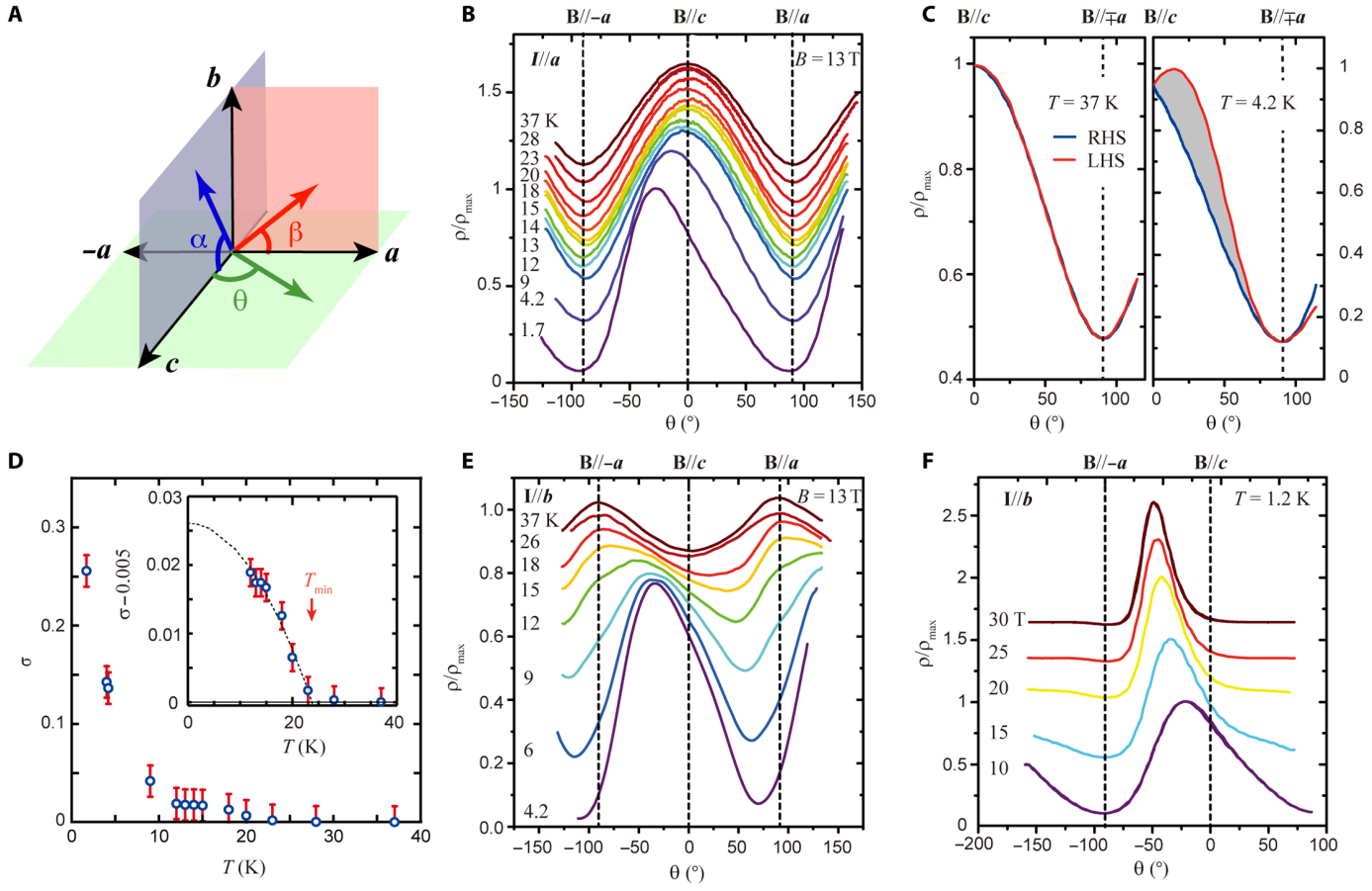

Fig. 2. Asymmetric MR of LMO within the *ac* plane. (**A**) Notation of angles for magnetic fields rotated within the three principal planes of the coordinate system specified in Fig. 1A. (**B**) Normalized ADMR curves obtained at various temperatures as a constant magnetic field of 13 T is rotated within the *ac* plane. The ADMR evolves from symmetric (about the *a* or the *c* axis) at high temperatures to asymmetric at low temperatures. Data are shifted vertically for clarity. Here, current is injected along the *a* axis. (**C**) Left panel: Mirror reflection of the ADMR curves at $T = 37$ K [in (A)] about the *c* axis. Right panel: Corresponding reflection plot at $T = 4.2$ K. The shaded region indicates the degree of asymmetry between these two curves. (**D**) Evolution of the asymmetric MR with temperature. The solid circles represent the degree of asymmetry in the ADMR, quantified by taking the normalized integrated area inside the red and blue curves in (B) defined as $\sigma \equiv (A_{LHS} - A_{RHS})/(A_{LHS} + A_{RHS})$. Inset: Blowup of the same figure between 10 and 40 K, to highlight the growth of the asymmetry below T_{min}. The dashed line is a fit to a simple parabolic temperature dependence. (**E**) Similar ADMR sweeps as in Fig. 2B, but for the current along the *b* axis, showing a similar asymmetry at low temperatures. (**F**) At a fixed temperature ($T = 1.2$ K), the asymmetry in the ADMR grows with increasing field.

the Lorentz force. With increasing field, the MR starts to deviate from its quadratic dependence and passes through a maximum at $B_{peak} \sim 14$ T (for **B**//*c*), indicating the emergence of a negative MR component to $\Delta\rho(B)$.

As the field is tilted away from the *c* axis, the low-field MR decreases in magnitude. Despite this decrease however, the peak in the MR actually shifts to a higher field, leading to a cascade of crossing points as displayed in Fig. 3A. As a consequence, the angle at which $\Delta\rho$ peaks (at constant field strength) shifts progressively away from the *c* axis with increasing field (Fig. 3B). Comparison of Fig. 3B with the ADMR data plotted in Fig. 2F confirms that the asymmetric MR in LMO arises because of the emergence of a negative component whose magnitude increases as the field is tilted away from a specific "critical angle" θ_{CR} within the *ac* plane. One might argue that a positive component peaking around θ_{CR} can also lead to the observed asymmetry. As discussed in our previous work (*17*), an anisotropic positive MR must arise because of the field-induced one-dimensionalization (i.e., decreased Fermi velocity along the *b* axis and, hence, enhanced scattering rate). Nevertheless, it is expected to preserve the mirror symmetry with respect to crystallographic axes rather than at an intermediate angle like θ_{CR}. As a result, this anisotropic positive MR, although being important to shape MR curves, cannot account for the observed asymmetry (see section S5 for further discussion of the anisotropic positive MR).

In Fig. 3C, the MR data are rescaled to remove the $|\cos\theta|$ dependence (as explained in section S2 and fig. S7). In this way, all the initial slopes collapse onto a single curve, as shown in the inset. Although the field scale has been substantially renormalized, the peak value B_{peak} plotted in Fig. 3D still exhibits its own maximum at a specific critical angle of $\theta_{CR} = -50° \pm 2°$ from the *c* axis. At this critical angle, the influence of the negative MR is, thus, at its weakest.

Inspection of the atomic configuration within the unit cell in Fig. 4A reveals that θ_{CR} corresponds very closely (in one of its two possible orientations) to an axis that passes directly through the poles of the MoO_6 octahedra [i.e., the interchain direction, conventionally denoted by [−2 0 1] as acknowledged previously in (*23*)]. From the

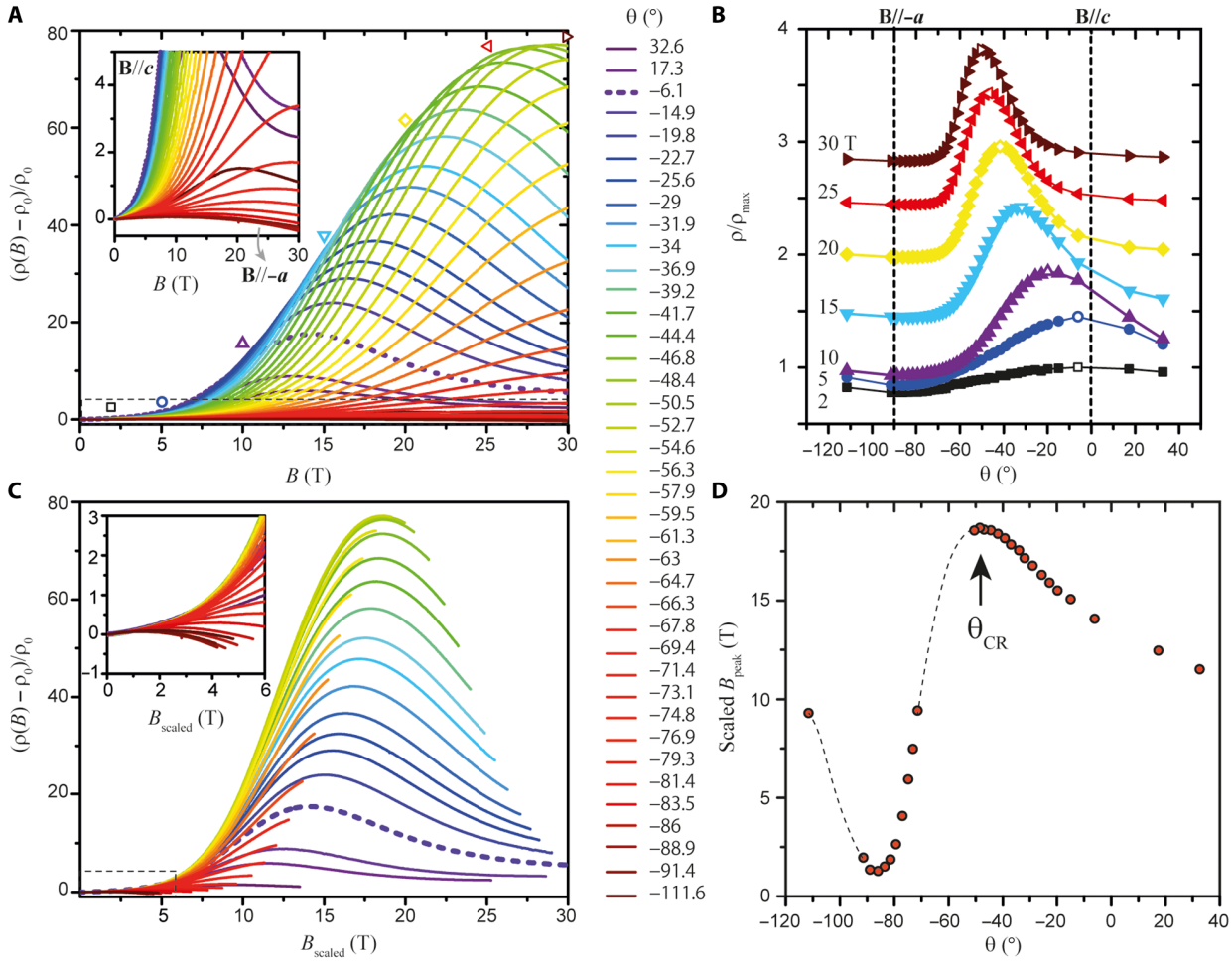

Fig. 3. Origin of the asymmetry and determination of the critical angle. (**A**) Field sweeps of the MR at 1.2 K are measured at various angles within the *ac* plane, showing the evolution of the peak field with angle. The angle of the dashed thick curve is ~6° from the *c* axis. The maximal MR at $B = 2$, 5, 10, 15, 20, 25, and 30 T are denoted by empty symbols and correspond to the peaks in (**B**). Inset: Expanded plot of the region of the MR curves contained below the dashed line in the main panel. (B) Same data as in (A), replotted for fixed field strengths. Each is vertically shifted for better visibility. Comparison with Fig. 2F shows almost identical behavior. (**C**) Same data as in (A) with the field values scaled by $|\cos\theta|$. The actual scaling factor, i.e., the ratio between B_{scaled} and B, is depicted in fig. S7. Inset: Expanded plot of the dashed rectangle in the main panel. (**D**) The resultant peak field values obtained from Fig. 3C plotted as a function of angle within the *ac* plane. At the critical angle θ_{CR}, the negative MR is maximally suppressed.

analysis presented in Fig. 3, we conclude that the negative MR contribution is minimized when the field is oriented along this specific polar axis, implying that the MR response of this bulk 3D crystal is governed by the real-space alignment of the atoms within the crystal lattice. Such a deviation in the symmetry of the MR from the crystal main axes may take place, for instance, in materials that are susceptible to a charge density wave (CDW) instability that is not necessarily aligned with the crystal main axis. In this case however, the asymmetry can be deduced almost entirely from the nesting conditions defined by the Fermi surface (*33*). Another example is a material with strong (e.g., Hubbard type) localization where, because electrons or holes spend most of their lifetime in the local atomic orbitals, it makes sense that the characteristics of local orbitals in real space become dominant. The uniqueness of LMO thus stems from the fact that in this system, which is nonetheless described well by itinerant electron physics, a signal is detected that can be ascribed directly to the local system of coordinates of atomic orbitals. Below, we introduce a model that can qualitatively explain this unprecedented effect.

DISCUSSION

In previous theoretical treatments of the TLL physics of LMO, only the pure d_{xy} orbitals were considered as a key starting ingredient (an assumption justified by the fact that only these cross E_F) (*30*, *34*). Recently however, other orbital degrees of freedom, in particular the interorbital interactions of the d_{xz} and d_{yz} orbitals, were incorporated into the many-body formalism and shown to affect the low-energy physics (*26*) (further details of the model are expounded in section S4). In particular, the specific arrangement of the d_{iz}-derived bands provides favorable conditions for the formation of excitons along the P-K line (highlighted in green in the lower panel of Fig. 1C). This exciton resides in adjacent octahedra within the two zigzag chains. The interband exciton has a spin triplet configuration that strongly suppresses the electron-hole recombination probability through photon emission and gives the resulting dark exciton a long lifetime (and allows for spin exchange scattering with the d_{xy} fermions). At high temperatures, excitons behave as free particles (with a hopping energy of the order 1 to 2 meV), while at low temperatures, the physics of these emergent particles is governed

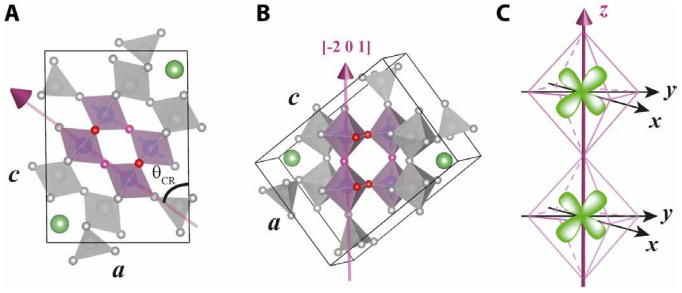

Fig. 4. Identification of the critical angle. (**A**) Blowup of the unit cell of LMO showing the alignment of the critical angle θ_{CR} (purple arrow) with the polar axis of the MoO_6 octahedra. (**B**) Rotation of the unit cell's frame of reference to the polar axis. (**C**) A pair of MoO_6 octahedra showing the orientation of the d_{yz} orbitals along this polar axis. A dark exciton, composed of d_{yz} (in green) and d_{xz} (not shown) orbitals, is formed in adjacent octahedra residing in two zigzag chains within a unit cell. Both orbitals have the same quantization axis (again indicated by the purple arrow). Crystallographic drawings were produced using VESTA (*44*).

by a quantum order-by-disorder transition (*35*), which leads to a Wigner-like periodic arrangement of the excitons. The d_{xy} fermions that remained mobile in the presence of the (slightly incommensurate) Umklapp processes associated with quarter-filling now localize on this additional potential, leading to an upturn in the resistivity below T_{min}.

Crucially, the angular momentum quantization axis for the dark excitons is the *z* axis of the local coordination system shown in Fig. 1B and indicated by the purple arrows in Fig. 4, A to C. Any component of the *B*-field perpendicular to this quantization axis will lead to a mixing of the d_{xz} and d_{yz} orbitals. This breaks the conservation of angular momentum, thereby admixing bright (via electron-hole recombination) and dark excitons and opening up their fast decay channel. Once the dark exciton—the essential building block of the Wigner crystal—acquires a finite lifetime, the crystal itself must melt. Ultimately, it is this melting of the excitonic order that suppresses the additional Umklapp process below T_{min}, giving rise to the negative MR and restoring the metallic state in the presence of a strong magnetic field (*17*). Since the crystal melting is strongly influenced by the angular offset between the magnetic field vector and the quantization axis, this model provides a natural explanation for the location of B_{peak} at $\theta = \theta_{CR}$ and the resulting asymmetric MR response; with decreasing temperature, the unique angular dependence is determined by the orientation of the *B*-field with respect to the quantization axis rather than to the main reciprocal axes of the lattice.

The fact that B_{peak} does not diverge at $\theta = \theta_{CR}$ is attributed within this picture to the slight canting of the MoO_6 octahedra within the unit cell $\phi_{cant} \sim 6°$, as illustrated in fig. S8 (and section S3), which ensures that there is always a residual component of the *B*-field that is orthogonal to the quantization axis and, thus, the condition for perfect alignment is never satisfied. When the magnetic field is rotated within the *ab* or *bc* plane, the angle between the *B*-field and the quantization axis is always maximized when **B**//*b*, and so is the negative MR (*17*, *26*). In addition, **B**//*a* and **B**//*c* have a higher positive MR than **B**//*b* due to the enhanced Lorentz force as well as a propensity for field-induced one-dimensionalization whenever the *B*-field is perpendicular to the atomic chains (*36*). Thus, one expects the maxima (minima) to be located at **B**//*a* or **B**//*c* (**B**//*b*), and no asymmetry in the ADMR is expected in these rotation planes (see section S5).

According to the theoretical model outlined above, the resistivity upturn in LMO is caused by a reentrance of Umklapp interactions between the remnant mobile d_{xy} fermions and this periodic [Wigner like (*37*)] arrangement of excitons (fig. S10). In one sense, the periodic arrangement of excitons helps to "complete" the Mott transition in near-commensurate LMO, i.e., the many body system uses its own multiorbital degrees of freedom to open a correlation gap and, hence, gain energy. Recalling that the formation of excitons is favored by long-range interactions and given that a 1D metal (in contrast to a metal in higher dimensions) is unable to screen long-range interactions, we conclude that this novel localization phenomenon can only take place in a 1D (Luttinger liquid) system–like LMO.

Now we return to discuss the unusual temperature dependence of the asymmetry parameter shown in Fig. 2B. According to the theory, not one single transition, but a sequence of two transitions (*38*, *39*), is expected. The first transition at $T = T_{min}$ is into a partially ordered state, while the second transition (into a fully frozen lattice) is expected to take place at $\sim T_{min}/3$, i.e., around 8 K. Furthermore, the magnitude of the order parameter associated with the intermediate phase order should be much smaller than the lowest-temperature fully ordered state. Both features are in agreement with the data presented in Fig. 2B.

Last, we turn to discuss various other mechanisms proposed for the resistivity upturn around T_{min} in the context of our new findings. The first is the CDW, possibly electronically driven (*23*), a suppression of which by Zeeman splitting in magnetic fields would lead to the giant negative MR (*17*). This suppression is expected to lead to an isotropic negative MR, however an expectation that is incompatible with the emerging symmetry axis unveiled by more detailed angular characterization in the present study. In the case of disorder-induced localization (*22*), the MR is also expected to display mirror symmetry within the *ac* plane, in notable contrast to the mirror symmetry–breaking response of the dark excitons that naturally correlates with the emerging symmetry axis. The dark exciton theory is, thus, expected to be an essential part of any mechanism accounting for the mysterious resistivity upturn, although how superconductivity develops with itinerant residual carriers in the presence of crystallized (localized) dark excitons is yet to be explored.

Mutual interplay between localized and itinerant degrees of freedom is a key issue in strongly correlated systems such as heavy fermions (*40*) and Kondo insulators (*41*). What happens when these two types of correlated carriers coexist, however, is largely uncharted territory, with no obvious guiding principles. Our experimental result, where both real and reciprocal space manifest in a single measurement, is likely to lay a new research direction in this field. The influence of the excitonic Wigner crystal on the magnetoresistive response of metallic LMO reported here is profound and is particularly notable given that it develops without a concomitant distortion of the lattice, suggesting that it is a purely electronically driven phenomenon. It turns out that the mysterious physics at T_{min} is driven by a type of order-by-disorder phase transition that has fascinated theorists for three decades. So far, however, the focus has been on spin systems. No one really looked at excitons as hardcore bosons, and this makes our result—a realization of such a transition in a simple transport experiment—so remarkable. Looking forward, it will be instructive to explore ways in which to detect these dark excitons directly [e.g., via low-energy electron diffraction (*42*) or resonant inelastic x-ray scattering (*43*)] and to investigate which other properties of LMO are influenced by their formation.

MATERIALS AND METHODS

Crystal growth and crystallographic characterization

High-quality single crystals of LMO were grown using a temperature gradient flux method, and their axes were identified by a Bruker

D8 QUEST single crystal x-ray diffractometer. Individual crystals were then blade cleaved within the *ab* plane to obtain thin, bar-shaped samples of approximate dimensions 600 μm by 200 μm by 40 μm.

Electrical measurement

Freshly cleaved samples were electronically connected by gold wires (50 μm in diameter) using silver paste (Dupont 4929N) before being mounted onto a rotary probe equipped with a Hall sensor and loaded into a temperature-variable cryostat inside a superconducting or Bitter magnet for low- and high-field measurements, respectively. A Keithley 6221 current source was used to generate an ac current excitation along the chosen axis, and a lock-in amplifier (Stanford Research 830) was used for the voltage measurement.

In a highly anisotropic crystal, accurate measurements of the electrical resistivity require careful consideration. For instance, to isolate the in-chain (diagonal) component of the electrical conductivity tensor, extreme care is needed to electrically short out the sample in the two directions perpendicular to the chain and, thus, ensure that current flow between the voltage contacts is uniaxial. In our experiments, this was achieved either by coating conductive paint or evaporating gold strips across the entire width of the sample in the two orthogonal current directions. The mounting configuration is shown in fig. S9. This configuration had been rigorously tested in a large number of LMO single crystals, which had led to consistent results for the absolute magnitudes of the resistivity along all three crystallographic axes, and their respective anisotropies showed excellent quantitative agreement with the measured anisotropy observed in both the optical conductivity (*22*) and the (square of the) upper critical field in superconducting LMO (*15*).

SUPPLEMENTARY MATERIALS

Supplementary material for this article is available at http://advances.sciencemag.org/cgi/content/full/5/7/eaar8027/DC1

Section S1. Similar observation in a superconducting sample (fig. S6)
Section S2. Scaling factor used in Fig. 3C and fig. S6C
Section S3. Canted angle between adjacent MoO_6 octahedra
Section S4. Theory of dark excitons and its contribution to resistivity and MR along the *a* axis
Section S5. Deconvolution of the anisotropic MR in LMO
Table S1. Location of the maxima and minima in the angular MR in LMO above T_{min}.
Fig. S1. Mirror reflection of the ADMR curves at various temperatures about the *c* axis.
Fig. S2. The magnitude of asymmetry as a function of temperature for MR curves of current along the *b* axis.
Fig. S3. Contrast in the asymmetric MR response upon rotation within the three crystallographic planes.
Fig. S4. Normalized ADMR curves obtained at various temperatures as a constant magnetic field of 13 T, rotated within the *bc* plane.
Fig. S5. Absence of asymmetric MR (*I*//*b*) with increasing field strength for *B* rotated within the *bc* plane.
Fig. S6. Origin of the asymmetric MR and determination of the critical angle for a second, superconducting LMO crystal.
Fig. S7. Scaling factor used in Fig. 3C and fig. S6C, respectively.
Fig. S8. A close view of the canted MoO_6 octahedra in LMO.
Fig. S9. Configurations of electric contacts applied to our LMO crystals.
Fig. S10. Schematic of crystallization of dark excitons.
Fig. S11. Power-law behavior of resistivity along the *b* axis in both insulating and superconducting LMO crystals.
References (*45*–*51*)

REFERENCES AND NOTES

1. M. N. Ali, J. Xiong, S. Flynn, J. Tao, Q. D. Gibson, L. M. Schoop, T. Liang, N. Haldolaarachchige, M. Hirschberger, N. P. Ong, R. J. Cava, Large, non-saturating magnetoresistance in WTe_2. *Nature* **514**, 205–208 (2014).
2. T. Liang, Q. Gibson, M. N. Ali, M. Liu, R. J. Cava, N. P. Ong, Ultrahigh mobility and giant magnetoresistance in the Dirac semimetal Cd_3As_2. *Nat. Mater.* **14**, 280–284 (2015).
3. C. Shekhar, A. K. Nayak, Y. Sun, M. Schmidt, M. Nicklas, I. Leermakers, U. Zeitler, Y. Skourski, J. Wosnitza, Z. Liu, Y. Chen, W. Schnelle, H. Borrmann, Y. Grin, C. Felser, B. Yan, Extremely large magnetoresistance and ultrahigh mobility in the topological Weyl semimetal candidate NbP. *Nat. Phys.* **11**, 645–649 (2015).
4. X. Huang, L. Zhao, Y. Long, P. Wang, D. Chen, Z. Yang, H. Liang, M. Xue, H. Weng, Z. Fang, X. Dai, G. Chen, Observation of the chiral-anomaly-induced negative magneto-resistance in 3D Weyl semi-metal TaAs. *Phys. Rev. X* **5**, 031023 (2015).
5. C.-L. Zhang, S. Y. Xu, I. Belopolski, Z. Yuan, Z. Lin, B. Tong, G. Bian, N. Alidoust, C.-C. Lee, S.-M. Huang, T.-R. Chang, G. Chang, C.-H. Hsu, H.-T. Jeng, M. Neupane, D. S. Sanchez, H. Zheng, J. Wang, H. Lin, C. Zhang, H.-Z. Lu, S.-Q. Shen, T. Neupert, M. Zahid Hasan, S. Jia, Signatures of the Adler–Bell–Jackiw chiral anomaly in a Weyl fermion semimetal. *Nat. Commun.* **7**, 10735 (2016).
6. X. Wang, Y. Du, S. Dou, C. Zhang, Room temperature giant and linear magnetoresistance in topological insulator Bi_2Te_3 nanosheets. *Phys. Rev. Lett.* **108**, 266806 (2012).
7. R. Xu, A. Husmann, T. F. Rosenbaum, M.-L. Saboungi, J. E. Enderby, P. B. Littlewood, Large magnetoresistance in non-magnetic silver chalcogenides. *Nature* **390**, 57–60 (1997).
8. T. Khouri, U. Zeitler, C. Reichl, W. Wegscheider, N. E. Hussey, S. Wiedmann, J. C. Maan, Linear magnetoresistance in a quasi-free two-dimensional electron gas in an ultrahigh mobility GaAs quantum well. *Phys. Rev. Lett.* **117**, 256601 (2016).
9. J.-M. Réau, C. Fouassier, P. Hagenmuller, Sur quelques nouveaux bronzes oxygènes de molybdène. *J. Solid State Chem.* **1**, 326–331 (1970).
10. J. Voit, One-dimensional Fermi liquids. *Rep. Prog. Phys.* **58**, 977–1116 (1995).
11. F. Wang, J. V. Alvarez, S.-K. Mo, J. W. Allen, G.-H. Gweon, J. He, R. Jin, D. Mandrus, H. Höchst, New Luttinger-liquid physics from photoemission on $Li_{0.9}Mo_6O_{17}$. *Phys. Rev. Lett.* **96**, 196403 (2006).
12. J. Hager, R. Matzdorf, J. He, R. Jin, D. Mandrus, M. A. Cazalilla, E. W. Plummer, Non-Fermi-liquid behavior in quasi-one-dimensional $Li_{0.9}Mo_6O_{17}$. *Phys. Rev. Lett.* **95**, 186402 (2005).
13. N. Wakeham, A. F. Bangura, X. Xu, J.-F. Mercure, M. Greenblatt, N. E. Hussey, Gross violation of the Wiedemann–Franz law in a quasi-one-dimensional conductor. *Nat. Commun.* **2**, 396 (2011).
14. M. Greenblatt, W. H. McCarroll, R. Neifeld, M. Croft, J. V. Waszczak, Quasi two-dimensional electronic properties of the lithium molybdenum bronze, $Li_{0.9}Mo_6O_{17}$. *Solid State Commun.* **51**, 671–674 (1984).
15. J.-F. Mercure, A. F. Bangura, X. Xu, N. Wakeham, A. Carrington, P. Walmsley, M. Greenblatt, N. E. Hussey, Upper critical magnetic field far above the paramagnetic pair-breaking limit of superconducting one-dimensional $Li_{0.9}Mo_6O_{17}$ single crystals. *Phys. Rev. Lett.* **108**, 187003 (2012).
16. C. Schlenker, H. Schwenk, C. Escribe-Filippini, J. Marcus, Superconducting properties of the low dimensional purple bronze $Li_{0.9}Mo_6O_{17}$. *Physica B+C* **135**, 511–514 (1985).
17. X. Xu, A. F. Bangura, J. G. Analytis, J. D. Fletcher, M. M. J. French, N. Shannon, J. He, S. Zhang, D. Mandrus, R. Jin, N. E. Hussey, Directional field-induced metallization of quasi-one-dimensional $Li_{0.9}Mo_6O_{17}$. *Phys. Rev. Lett.* **102**, 206602 (2009).
18. H. Chen, J. J. Ying, Y. L. Xie, G. Wu, T. Wu, X. H. Chen, Magnetotransport properties in purple bronze $Li_{0.9}Mo_6O_{17}$ single crystal. *EPL Europhys. Lett.* **89**, 67010 (2010).
19. M. S. da Luz, C. A. M. dos Santos, J. Moreno, B. D. White, J. J. Neumeier, Anisotropic electrical resistivity of quasi-one-dimensional $Li_{0.9}Mo_6O_{17}$ determined by the Montgomery method. *Phys. Rev. B* **76**, 233105 (2007).
20. J. L. Cohn, B. D. White, C. A. M. dos Santos, J. J. Neumeier, Giant Nernst effect and bipolarity in the quasi-one-dimensional metal $Li_{0.9}Mo_6O_{17}$. *Phys. Rev. Lett.* **108**, 056604 (2012).
21. G.-H. Gweon, J. W. Allen, J. D. Denlinger, Generalized spectral signatures of electron fractionalization in quasi-one- and two-dimensional molybdenum bronzes and superconducting cuprates. *Phys. Rev. B* **68**, 195117 (2003).
22. J. Choi, J. L. Musfeldt, J. He, R. Jin, J. R. Thompson, D. Mandrus, X. N. Lin, V. A. Bondarenko, J. W. Brill, Probing localization effects in $Li_{0.9}Mo_6O_{17}$ purple bronze: An optical-properties investigation. *Phys. Rev. B* **69**, 085120 (2004).
23. C. A. M. dos Santos, B. D. White, Y.-K. Yu, J. J. Neumeier, J. A. Souza, Dimensional crossover in the purple bronze $Li_{0.9}Mo_6O_{17}$. *Phys. Rev. Lett.* **98**, 266405 (2007).
24. J. Chakhalian, Z. Salman, J. Brewer, A. Froese, J. He, D. Mandrus, R. Jin, Magnetism in purple bronze $Li_{0.9}Mo_6O_{17}$. *Phys. B Condens. Matter* **359–361**, 1333–1335 (2005).
25. C. A. M. dos Santos, M. S. da Luz, Y.-K. Yu, J. J. Neumeier, J. Moreno, B. D. White, Electrical transport in single-crystalline $Li_{0.9}Mo_6O_{17}$: A two-band Luttinger liquid exhibiting Bose metal behavior. *Phys. Rev. B* **77**, 193106 (2008).
26. P. Chudziński, Multi-orbital physics in lithium-molybdenum purple-bronze: Going beyond paradigm. *Eur. Phys. J. B.* **90**, 148 (2017).
27. E. Poem, Y. Kodriano, C. Tradonsky, N. H. Lindner, B. D. Gerardot, P. M. Petroff, D. Gershoni, Accessing the dark exciton with light. *Nat. Phys.* **6**, 993–997 (2010).
28. M. Onoda, K. Toriumi, Y. Matsuda, M. Sato, Crystal structure of lithium molybdenum purple bronze $Li_{0.9}Mo_6O_{17}$. *J. Solid State Chem.* **66**, 163–170 (1987).
29. M. H. Whangbo, E. Canadell, Band electronic structure of the lithium molybdenum purple bronze $Li_{0.9}Mo_6O_{17}$. *J. Am. Chem. Soc.* **110**, 358–363 (1988).

30. Z. S. Popović, S. Satpathy, Density-functional study of the Luttinger liquid behavior of the lithium molybdenum purple bronze $Li_{0.9}Mo_6O_{17}$. *Phys. Rev. B* **74**, 045117 (2006).
31. M. Nuss, M. Aichhorn, Effective model for the electronic properties of quasi-one-dimensional purple bronze $Li_{0.9}Mo_6O_{17}$ based on ab initio calculations. *Phys. Rev. B* **89**, 045125 (2014).
32. D. Graf, J. S. Brooks, E. S. Choi, M. Almeida, R. T. Henriques, J. C. Dias, S. Uji, Geometrical and orbital effects in a quasi-one-dimensional conductor. *Phys. Rev. B* **80**, 155104 (2009).
33. H. Guyot, J. Dumas, M. V. Kartsovnik, J. Marcus, C. Schlenker, I. Sheikin, D. Vignolles, Angular studies of the magnetoresistance in the density wave state of the quasi-two-dimensional purple bronze KMo_6O_{17}. *Eur. Phys. J. B.* **58**, 25–30 (2007).
34. P. Chudziński, T. Jarlborg, T. Giamarchi, Luttinger-liquid theory of purple bronze $Li_{0.9}Mo_6O_{17}$ in the charge regime. *Phys. Rev. B* **86**, 075147 (2012).
35. A. G. Green, G. Conduit, F. Krüger, Quantum order-by-disorder in strongly correlated metals. *Annu. Rev. Condens. Matter Phys.* **9**, 59–77 (2018).
36. L. P. Gor'kov, A. G. Lebed, On the stability of the quasi-one dimensional metallic phase in magnetic fields against the spin density wave formation. *J. Phys. Lett.* **45**, 433–440 (1984).
37. C. C. Grimes, G. Adams, Evidence for a liquid-to-crystal phase transition in a classical, two-dimensional sheet of electrons. *Phys. Rev. Lett.* **42**, 795–798 (1979).
38. D. Blankschtein, M. Ma, A. N. Berker, G. S. Grest, C. M. Soukoulis, Orderings of a stacked frustrated triangular system in three dimensions. *Phys. Rev. B* **29**, 5250–5252 (1984).
39. R. Moessner, S. L. Sondhi, Ising models of quantum frustration. *Phys. Rev. B.* **63**, 224401 (2001).
40. J. A. Mydosh, P. M. Oppeneer, Hidden order behaviour in URu_2Si_2. *Philos. Mag.* **94**, 3642–3662 (2014).
41. P. Coleman, *Heavy Fermions: Electrons at the edge of magnetism, volume 1* of Handbook of Magnetism and Advanced Magnetic Materials (John Wiley Sons, 2007).
42. F. Jona, J. A. Strozier Jr., W. S. Yang, Low-energy electron diffraction for surface structure analysis. *Rep. Prog. Phys.* **45**, 527 (1982).
43. L. J. P. Ament, M. van Veenendaal, T. P. Devereaux, J. P. Hill, J. van den Brink, Resonant inelastic x-ray scattering studies of elementary excitations. *Rev. Mod. Phys.* **83**, 705–767 (2011).
44. K. Momma, F. Izumi, VESTA 3 for three-dimensional visualization of crystal, volumetric and morphology data. *J. Appl. Cryst.* **44**, 1272–1276 (2011).
45. R. Moessner, J. T. Chalker, Low-temperature properties of classical geometrically frustrated antiferromagnets. *Phys. Rev. B* **58**, 12049–12062 (1998).
46. J. V. José, L. P. Kadanoff, S. Kirkpatrick, D. R. Nelson, Renormalization, vortices, and symmetry-breaking perturbations in the two-dimensional planar model. *Phys. Rev. B* **16**, 1217–1241 (1977).
47. A. O. Gogolin, A. A. Nersesyan, A. M. Tsvelik, *Bosonization and Strongly Correlated Systems* (Cambridge Univ. Press, 2004).
48. J. Choi, J. D. Woodward, J. L. Musfeldt, X. Wei, M.-H. Whangbo, J. He, R. Jin, D. Mandrus, Magneto-optical properties of $Li_{0.9}Mo_6O_{17}$: Color change in applied magnetic field. *Phys. Rev. B* **70**, 085107 (2004).
49. J. L. Cohn, P. Boynton, J. S. Triviño, J. Trastoy, B. D. White, C. A. M. dos Santos, J. J. Neumeier, Stoichiometry, structure, and transport in the quasi-one-dimensional metal $Li_{0.9}Mo_6O_{17}$. *Phys. Rev. B* **86**, 195143 (2012).
50. N. Dupuis, G. Montamboux, Localization and magnetic field in a quasi-one-dimensional conductor. *Phys. Rev. B* **46**, 9603 (1992).
51. A. Narduzzo, A. Enayati-Rad, P. J. Heard, S. L. Kearns, S. Horii, F. F. Balakirev, N. E. Hussey, Fragile three-dimensionality in the quasi-one-dimensional cuprate $PrBa_2Cu_4O_8$. *New J. Phys.* **8**, 172–179 (2006).

Acknowledgments: We acknowledge enlightening discussions with A. Ho, J. Quintanilla, and M. Katsnelson. **Funding:** We also acknowledge the support of the HFML-RU/NWO, a member of the European Magnetic Field Laboratory (EMFL). This work forms part of the research program "Strange Metals" (grant no. 16METL01, 2017–2021) of the former Foundation for Fundamental Research on Matter (FOM), which is financially supported by the Netherlands Organisation for Scientific Research (NWO). Part of this work was also supported by the National Natural Science Foundation of China grant no. U1732162 (2018–2020) entitled "Quantum transport of quasi-one-dimensional superconductors under high magnetic field." M.G. acknowledges support of NSF-DMR 1507252 grant (2015–2019) entitled "Multifunctional transition metal compounds with correlated electronic properties: Synthesis and characterization." **Author contributions:** The experiment was conceived by N.E.H., X.X., J.L., and P.C. J.L. and X.X. performed the measurements, with assistance from S.L., M.R.v.D., and J.B. M.G. and R.J. provided crystals, while P.T. performed x-ray crystallographic analysis. The manuscript was prepared by N.E.H., J.L., X.X., and P.C., with input from all the other co-authors. **Competing interests:** The authors declare that they have no competing interests. **Data and materials availability:** All data needed to evaluate the conclusions in the paper are present in the paper and/or the Supplementary Materials. Additional data related to this paper may be requested from the authors.

Submitted 19 December 2017
Accepted 29 May 2019
Published 5 July 2019
10.1126/sciadv.aar8027

Citation: J. Lu, X. Xu, M. Greenblatt, R. Jin, P. Tinnemans, S. Licciardello, M. R. van Delft, J. Buhot, P. Chudzinski, N. E. Hussey, Emergence of a real-space symmetry axis in the magnetoresistance of the one-dimensional conductor $Li_{0.9}Mo_6O_{17}$. *Sci. Adv.* **5**, eaar8027 (2019).